JGR

Data-driven Green's function retrieval and application to imaging with multidimensional deconvolution

Filippo Broggini[1,2], Kees Wapenaar[3], Joost van der Neut[3], and Roel Snieder[1]

[1]Center for Wave Phenomena, Colorado School of Mines, Golden, Colorado, USA [2]Now at Institute of Geophysics, ETH Zürich, Zürich, Switzerland [3]Department of Geoscience and Engineering, Delft University of Technology, Delft, Netherlands

Abstract An iterative method is presented that allows one to retrieve the Green's function originating from a virtual source located inside a medium using reflection data measured only at the acquisition surface. In addition to the reflection response, an estimate of the travel times corresponding to the direct arrivals is required. However, no detailed information about the heterogeneities in the medium is needed. The iterative scheme generalizes the Marchenko equation for inverse scattering to the seismic reflection problem. To give insight in the mechanism of the iterative method, its steps for a simple layered medium are analyzed using physical arguments based on the stationary phase method. The retrieved Green's wavefield is shown to correctly contain the multiples due to the inhomogeneities present in the medium. Additionally, a variant of the iterative scheme enables decomposition of the retrieved wavefield into its downgoing and upgoing components. These wavefields then enable creation of a ghost-free image of the medium with either cross correlation or multidimensional deconvolution, presenting an advantage over standard prestack migration.

1. Introduction

One of the main goals of seismic imaging is to retrieve the location and amplitude of reflectors in the subsurface from reflection data acquired on the surface of the Earth. This is an important and challenging task because an accurate image of the structures inside the Earth is needed to locate hydrocarbon reservoirs.

We discuss a new approach to retrieve the full-waveform Green's function originating from a virtual source located inside a medium using only reflection data measured at the acquisition surface. Existing methods, such as seismic interferometry [*Bakulin and Calvert*, 2006; *Schuster*, 2009], allow one to retrieve this Green's wavefield without any knowledge of the medium itself. Despite their advantages, these methods are affected by two major drawbacks: (1) they require a receiver (or a source) at the location of the virtual source (or receiver) in the subsurface and (2) they assume the medium is surrounded by sources (or receivers). Our approach removes these constraints and is based on an extension of the one-dimensional theory proposed by *Broggini et al.* [2011, 2012] and *Broggini and Snieder* [2012], both based, in turn, on earlier work by *Rose* [2002]. They show that, given the reflection response of a one-dimensional layered medium, it is possible to retrieve the response to a virtual source inside the medium, without having a receiver at the virtual source location and without knowing the medium. *Wapenaar et al.* [2013] generalized this to three-dimensional media. This new method consists of an iterative algorithm that transforms the reflection response (at the acquisition surface) of an arbitrary medium into the wavefield generated by a virtual source inside the unknown medium. This can be interpreted as a redatuming process. Apart from requiring the reflection data measured at the surface, the proposed method also requires an estimate of the travel times of the first arriving wave traveling from the virtual source location to receivers located at the acquisition surface. These travel times are a key element of the method because they specify the location of the virtual source in the subsurface. Consequently, the proposed method is not fully model independent. However, we do not require any more knowledge of the medium parameters than standard primary imaging schemes. As in seismic interferometry [*Curtis et al.*, 2006, *Schuster*, 2009], our goal is to retrieve the response to a virtual source inside an unknown medium, removing the imprint of a complex subsurface. This is helpful in situations where waves have traversed a strongly inhomogeneous overburden, e.g., subsalt [*Sava and Biondi*, 2004] and for near-surface imaging [*Keho and Kelamis*, 2012].

The main aim of this paper is to provide insight in the mechanism of the new method, by applying it to a relatively simple configuration. Following the approach of *Wapenaar et al.* [2012a], we analyze the iterative
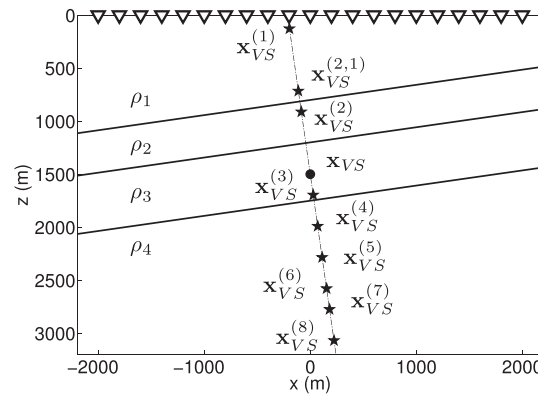
Figure 1. Configuration with three dipping reflectors. The black dot indicates the location of the virtual source $\mathbf{x}_{VS}$. The black star-shaped symbols indicate the locations of the mirror images of the virtual source. $\mathbf{x}_{VS}^{(2,1)}$ is the mirror image of $\mathbf{x}_{VS}^{(2)}$ with respect to the first reflector. The white triangles denote the receivers at $z = 0$. The virtual source and its mirror images lie on the line $z = z_{VS} + x/a$, with $z_{VS} = 1500$ m and $a = 1/7$.

method for a layered configuration with three-parallel dipping reflectors characterized by variable density and constant velocity. We use physical arguments based on the stationary phase method to show that the method converges and allows for the retrieval of the wavefield originating from the virtual source location. Then, we show that a variant of the iterative scheme allows us to decompose the retrieved Green's function into its downgoing and upgoing components. Finally, these decomposed wavefields are used to create an internal multiple free image of the subsurface. This image is constructed using either simple cross correlations or multidimensional deconvolution and is compared to standard prestack migration [*Claerbout*, 1985].

2. Stationary Phase Analysis

We discuss the proposed iterative scheme for a simple two-dimensional configuration. We use a geometrical approach to the method of stationary phase to solve the Rayleigh-like integrals which yield the reflected response to an arbitrary incident field. We explain each step of the iterative procedure and emphasize the physical arguments that support our expectations for the method to converge to the virtual-source response.

2.1. Configuration

We consider a model characterized by three parallel dipping reflectors in a lossless, constant-velocity, variable-density medium as shown in Figure1. The proposed iterative scheme is, however, not restricted to a medium where the velocity does not vary in space [*Wapenaar et al.*, 2013]. We choose this particular configuration because well-known analytical equations describe the wavefields propagating in constant-velocity media. The velocity of the medium is equal to $c = 2000$ m/s. We denote spatial coordinates as $\mathbf{x} = (x, z)$. The acquisition surface is located at $z = 0$ m and does not correspond to an actual reflector; hence, it does not cause reflections. The reflector at the top is described by the equation $z = z_1 - ax$ with $z_1 = 800$ m and $a = 1/7$. The black dot denotes the position of the virtual source, with coordinates $\mathbf{x}_{VS} = (x_{VS}, z_{VS}) = (0, 1500)$ m. The middle and bottom reflectors are characterized by the same dipping angle. For this reason, all mirror images of the virtual source are located on a line orthogonal to the reflectors. All the points on this line satisfy the relation $z = z_{VS} + x/a$. The first, second, and third reflectors cross this line at $\mathbf{x}_1 = (-98, 814)$ m, $\mathbf{x}_2 = (-42, 1206)$ m, and $\mathbf{x}_3 = (35, 1745)$ m, respectively. The densities in the four layers are $\rho_1 = \rho_3 = 1000$ kg/m³, $\rho_2 = 5000$ kg/m³, and $\rho_4 = 3000$ kg/m³, respectively. When a downgoing wave reaches one of the boundaries separating layers with different density, it gives rise to reflected and transmitted waves. The reflection and transmission coefficients are defined by $r_n = (\rho_{n+1} - \rho_n)/(\rho_{n+1} + \rho_n)$ and $\tau_n^+ = 1 + r_n$, respectively, where $n = 1, 2, 3$ denotes the layer. Similarly, the reflection and transmission coefficients for upgoing waves are $-r_n$ and $\tau_n^- = 1 - r_n$. Since the velocity is constant in this particular configuration, the reflection and transmission coefficients hold not only for normal incidence but for all the angles of incidence. Note that the large contrast between the density of the layers causes strong multiple reflections.
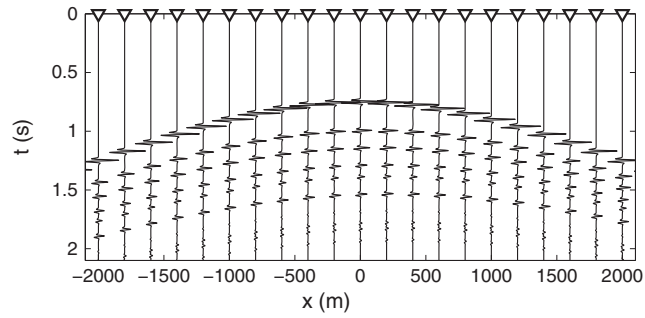
Figure 2. Total field originated by a real source located at $\mathbf{x}_{vs}$, i.e., $G(\mathbf{x}, \mathbf{x}_{vs}, t) * s(t)$. This is the reference wavefield.

2.2. Primary Arrivals

We define the Green's function $G(\mathbf{x}, \mathbf{x}_s, t)$ as a wavefield that satisfies the wave equation $LG = -\rho\delta(\mathbf{x} - \mathbf{x}_s)\frac{\partial\delta(t)}{\partial t}$, with $L = \rho\nabla \cdot (\rho^{-1}\nabla) - c^{-2}\frac{\partial 2}{\partial t2}$. According to *de Hoop* [1995], the Green's function corresponds to the response to an impulsive point source of volume injection rate located at x_s. Figure 2 shows the total field originated by a real source located at $\mathbf{x}_{vs}$, i.e., $G(\mathbf{x}, \mathbf{x}_{vs}, t) * s(t)$, where $s(t)$ is a Ricker wavelet with a central frequency of 15 Hz and $*$ denotes temporal convolution. This is the reference wavefield that we want to retrieve. It is essential that $s(t)$ is zero phase because the proposed method combines causal signals with time-reversed ones; see section 2.5. Using the Fourier convention $\hat{F}(\omega) = \int_{-\infty}^{+\infty} f(t) \exp(-j\omega t)dt$, the frequency domain Green's function $\hat{G}(\mathbf{x}, \mathbf{x}_s, \omega)$ obeys the equation $\hat{L}\hat{G} = -j\omega\rho\delta(\mathbf{x} - \mathbf{x}_s)$, with $\hat{L} = \rho\nabla \cdot (\rho^{-1}\nabla) + \omega^2/c^2$. Here j is the imaginary unit, and ω denotes the angular frequency. We decompose the Green's function in its direct and scattered components, $\hat{G} = \hat{G}^d + \hat{G}^s$.

As mentioned in section 1, we need an estimate of the direct arrivals. For the simple configuration of Figure 1, where there are only variations in density, the high-frequency approximation of the Fourier transform of the direct Green's function $G^d(\mathbf{x}, \mathbf{x}_{vs}, t)$ is given by

$$\hat{G}^d(\mathbf{x}, \mathbf{x}_{vs}, \omega) = \tau_1^- \tau_2^- \rho_3 j\omega \frac{\exp\left\{-j(\omega|\mathbf{x} - \mathbf{x}_{vs}|/c + \mu\pi/4)\right\}}{\sqrt{8\pi|\omega||\mathbf{x} - \mathbf{x}_{vs}|/c}},\tag{1}$$

where $\mu = \text{sign}(\omega)$ [*Snieder*, 2004]. Its temporal counterpart $G^d(\mathbf{x}, \mathbf{x}_{vs}, t)$, convolved with $s(t)$, is shown in Figure 3. In Figure 3, we also define two travel time curves indicated by the solid black lines. The lower curve describes the onset time of the direct arrivals, and the upper curve is defined as the time reversal of the lower curve. These two curves allow us to define a window function

$$w(\mathbf{x}, t) = 1 \quad \text{between the solid black lines of Figure 3,}$$

$$w(\mathbf{x}, t) = 0 \quad \text{elsewhere.}\tag{2}$$

This window function is a key component of the iterative scheme.
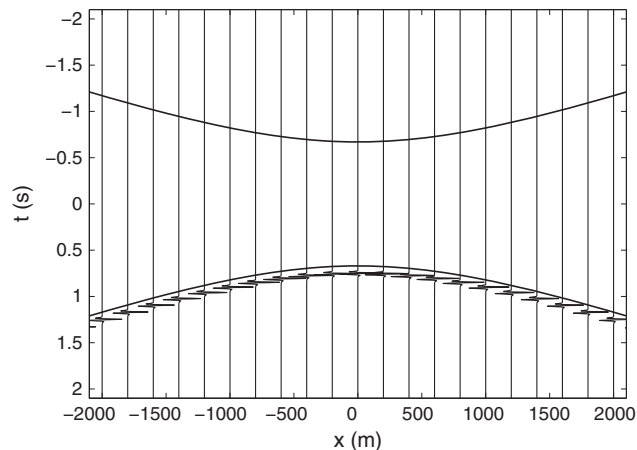

Figure 3. Direct arrivals of the response to the virtual source $\mathbf{x}_{vs}$ measured at the acquisition surface. The bottom solid black line indicates the onset time of the direct arrivals. The top solid black line is the time-reversed version of the bottom black line.
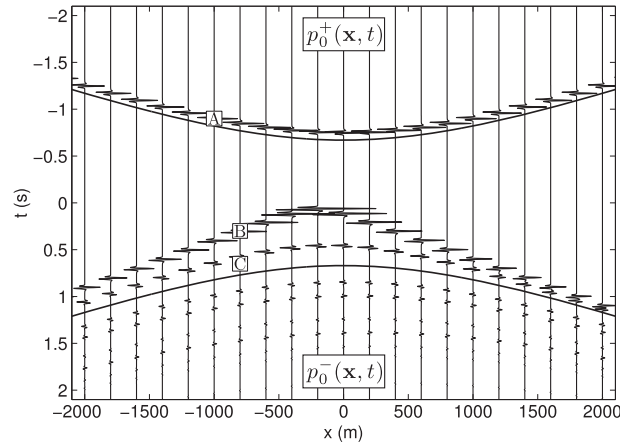
Figure 4. Initial incident wavefield ($t < 0$) and its reflection response ($t > 0$), both measured at $z = 0$. Initial incident wavefield is a scaled version of the time reversal of Figure 3 (see equations (5) and (6)). We show the reflection response only until 2 s. The solid black lines denote the onset time of the direct arrivals and its time-reversed counterpart. These black lines are repeated in the subsequent figures.

2.3. Reflection Response

To retrieve the virtual-source response $G(\mathbf{x}, \mathbf{x}_{VS}, t)$, we need the reflection response at the surface $R(\mathbf{x}_R, \mathbf{x}_S, t) * s(t)$ in addition to an estimate of the direct arrivals. We assume that the reflection data do not include any multiples related to the acquisition surface. Additionally, the source wavelet should be deconvolved from the reflection response. If surface-related multiples are present in the reflection data, then they must be removed with an appropriate technique [*Verschuur et al.*, 1992; *Amundsen*, 2001; *Groenestijn and Vershuur*, 2009]. Following *Wapenaar and Berkhout* [1993] (equation (15a)), an expression for the reflection response can be derived from a Rayleigh-type integral:

$$\hat{p}^-(\mathbf{x}_R, \omega) = \int_{-\infty}^{\infty} \frac{2}{j\omega\rho_1} \left[\frac{\partial \hat{G}^s(\mathbf{x}_R, \mathbf{x}, \omega)}{\partial z} \hat{p}^+(\mathbf{x}, \omega) \right]_{z=0} \mathrm{d}x, \tag{3}$$

where $\hat{p}^+$ and $\hat{p}^-$ are the Fourier transform of the downgoing and upgoing wavefields, respectively. Hence, in the frequency domain, we define the reflection response in terms of the scattering Green's function $\hat{G}^s$ via

$$\hat{R}(\mathbf{x}_R, \mathbf{x}_S, \omega)\hat{s}(\omega) = \frac{2}{j\omega\rho_1} \frac{\partial \hat{G}^s(\mathbf{x}_R, \mathbf{x}_S, \omega)}{\partial z_S} \hat{s}(\omega), \tag{4}$$

for $z_R = z_S = 0$ and after multiplying both sides by the spectrum of the source wavelet $s(t)$. According to *Berkhout* [1987], $\hat{R}(\mathbf{x}_R, \mathbf{x}_S, \omega)\hat{s}(\omega)$ is equivalent to the pressure recorded at $\mathbf{x}_R$ due to a unidirectional point force source oriented in the vertical direction located at $\mathbf{x}_S$ and multiplied by -2.

2.4. Initiating the Iterative Process

We define the initial incident downgoing wavefield at $z = 0$ as the inverse of the direct arrival of the transmission response $\mathcal{T}^d(\mathbf{x}_{VS}, \mathbf{x}, t)$, convolved with the wavelet $s(t)$; hence, $p_0^+(\mathbf{x}, t) = \{\mathcal{T}^d(\mathbf{x}_{VS}, \mathbf{x}, t)\}^{-1} * s(t)$. This transmission response is related to the vertical derivatives of the direct Green's function at $z = 0$ and z_{VS} (see K. Wapenaar et al., Green's function retrieval from reflection data, in absence of a receiver at the virtual source position, submitted to *Journal of the Acoustical Society of America*, 2014, Appendix A). For the high-frequency regime, we approximate the inverse transmission response by a scaled version of the time-reversed version of the direct Green's function; hence,

$$p_0^+(\mathbf{x}, t) = G_0^d(\mathbf{x}, \mathbf{x}_{VS}, -t) * s(t), \tag{5}$$

with

$$G_0^d(\mathbf{x}, \mathbf{x}_{VS}, t) = \left(\tau_1^+ \tau_1^- \tau_2^+ \tau_2^- \right)^{-1} G^d(\mathbf{x}, \mathbf{x}_{VS}, t), \tag{6}$$

where the amplitude scalar multiplying G^d compensates for the effect of transmission losses at the interfaces. The initial wavefield $p_0^+(\mathbf{x}, t)$ is shown in Figure 4 with the label A. The subscript 0 of $p_0^+(\mathbf{x}, t)$ indicates the initial wavefield (or the 0th iteration).
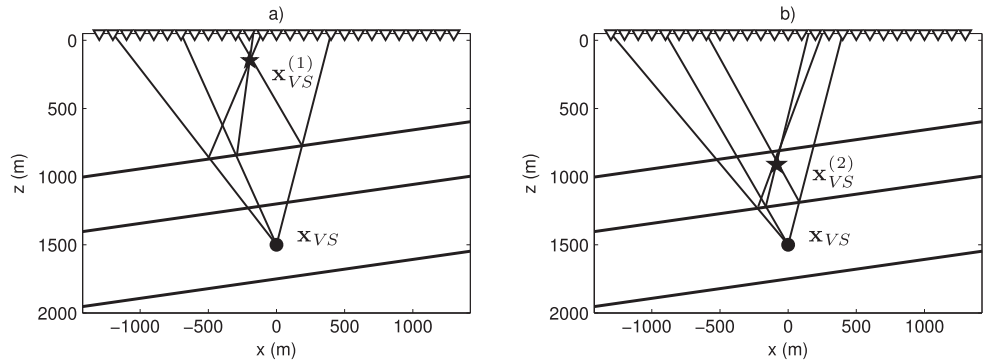
Figure 5. Analysis of the response of the first and second reflectors to the initial incident wavefield $p_0^+(\mathbf{x}, t)$. (a) Stationary rays for different receivers. The response of the first reflector seems to originate from $\mathbf{x}_{VS}^{(1)}$. (b) Stationary rays for different receivers. The response of the second reflector seems to originate from $\mathbf{x}_{VS}^{(2)}$.

The reflected upgoing wavefield $p_0^-(\mathbf{x}, t)$ is obtained by convolving the downgoing incident wavefield $p_0^+(\mathbf{x}, t)$ with the deconvolved reflection response and integrating over the source locations:

$$p_0^-(\mathbf{x}_R, t) = \int_{-\infty}^{\infty} \left[R(\mathbf{x}_R, \mathbf{x}, t) * p_0^+(\mathbf{x}, t) \right]_{z=0} dx, \tag{7}$$

for $z_R = 0$. Equation (7) is the time domain version of the Rayleigh integral described by equation (3). We discuss and solve this integral with geometrical arguments based on the method of stationary phase, and we give a detailed mathematical derivation in the Appendix A. Figure 5 shows various rays for different receiver locations. Note that the rays of the incident field (converging in $\mathbf{x}_{VS}$) and of the reflection response (for the first reflector) have the same direction [see *Wapenaar et al.*, 2010, Appendix]. For this reason, these specific rays are said to be stationary. With simple geometrical arguments, it follows that these rays cross each other at the mirror image of the virtual source with respect to the first reflector, i.e., at $\mathbf{x}_{VS}^{(1)}$. Hence, the response of the first dipping reflector to the initial downgoing field appears to originate from a virtual source located at $\mathbf{x}_{VS}^{(1)}$. This wavefield corresponds to $r_1 G_0^d(\mathbf{x}_R, \mathbf{x}_{VS}^{(1)}, t) * s(t)$, the first term on the right-hand side of equation (A21), and is shown as the event with label B in Figure 4. Following similar stationary phase arguments, the response of the second reflector to the initial downgoing field apparently originates from a mirror image of the virtual source with respect to the second reflector, i.e., at $\mathbf{x}_{VS}^{(2)}$. This response is equal to $\tau_1^- r_2 \tau_1^+ G_0^d(\mathbf{x}_R, \mathbf{x}_{VS}^{(2)}, t) * s(t)$ and corresponds to the second term on the right-hand side of equation (A21) (see the event with label C in Figure 4). However, the multiply reflected responses to the initial incident field also apparently originate from mirror images of the virtual source, all located along the line $z = z_{VS} + x/a$ (see Figure 1). We derived these responses with the method of stationary phase; hence, they are free of finite-aperture artifacts. We emphasize that the stationary phase analysis is not essential for the method, but it is used here because the wavefields obey simple analytical expressions.

2.5. Iterative Process

We now discuss an iterative scheme, which uses the (k-1)th iteration of the reflection response $p_{k-1}^-(\mathbf{x}, t)$ to create the kth iteration of the incident field $p_k^+(\mathbf{x}, t)$. The objective is to iteratively update the incident field in such a way that, within the region between the upper and lower solid black lines shown in Figure 4, the field becomes antisymmetric in time. The meaning of this criterion will be evident in the next section, where we show how to retrieve $G(\mathbf{x}, \mathbf{x}_{VS}, t)$. The method requires a combination of time reversal and windowing, and the kth iteration of the incident field is defined by

$$p_k^+(\mathbf{x}, t) = p_0^+(\mathbf{x}, t) - w(\mathbf{x}, t) p_{k-1}^-(\mathbf{x}, -t), \text{ for } \mathbf{x} \text{ at } z = 0, \tag{8}$$

where the time window $w(\mathbf{x}, t)$ is defined by equation (2). The reflection response is then obtained using equation (7), which we rewrite here as

$$p_k^-(\mathbf{x}_R, t) = \int_{-\infty}^{\infty} \left[R(\mathbf{x}_R, \mathbf{x}, t) * p_k^+(\mathbf{x}, t) \right]_{z=0} dx, \tag{9}$$

for $\mathbf{x}$ and $\mathbf{x}_R$ at $z = 0$. The first and second iterations of the incident and reflected fields are shown in Figures 6 and 7, respectively. The events of $p_1^+(\mathbf{x}, t)$ labeled B and C in Figure 6 correspond to the events of $p_0^-(\mathbf{x}, t)$
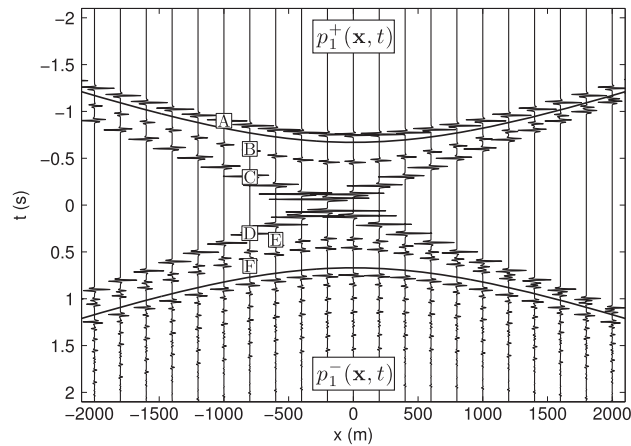
Figure 6. First iteration of the incident wavefield ($t < 0$) and its reflection response ($t > 0$), both measured at $z = 0$. The labels A−F identify the first six events in the total field. We show the reflection response only until 2 s.

labeled C and B in Figure 4 (time reversed and multiplied by -1; see equation (8)). Similarly, the events of $p_2^+(\mathbf{x}, t)$ labeled B, C, and D in Figure 7 correspond to the events of $p_1^-(\mathbf{x}, t)$ labeled F, E, and D in Figure 6 (time reversed and multiplied by -1).

For this particular configuration, the kth iteration of the incident field (for $k > 2$) is similar to $p_2^+(\mathbf{x}, t)$ and is composed of four events, as shown in Figure 7 for $t < 0$. The events labeled A and D remain unchanged in the iterative process. The other two events (labeled B and C) correspond to $-A_k^{(2)} G_0^d(\mathbf{x}_R, \mathbf{x}_{VS}^{(2)}, -t) * s(t)$ and $-A_k^{(2,1)} G_0^d(\mathbf{x}_R, \mathbf{x}_{VS}^{(2,1)}, -t) * s(t)$, respectively. $\mathbf{x}_{VS}^{(2,1)}$ is the mirror image of $\mathbf{x}_{VS}^{(2)}$ with respect to the first reflector. The coefficient $A_k^{(2)}$ varies at each iteration and is equal to the partial sum of the geometric series $b + by + by^2 + by^3 + by^4 + \cdots + by^k$ where $b = \tau_1^+ r_2 \tau_1^-$ and $y = r_1^2$. The sum of the series converges because $y < 1$ and yields

$$\sum_{k=0}^{\infty} by^k = \frac{b}{1-y} = r_2, \tag{10}$$

where we used that $1 - r_1^2 = \tau_1^- \tau_1^+$. The coefficient $A_k^{(2,1)}$ of the third event (labeled C in Figure 7) is equal to $-r_1 A_k^{(2)}$; and hence, it converges to $-r_1 r_2$. Figure 8 shows the thirtieth iteration, and within the solid black lines, the wavefield is antisymmetric in time. This is the result we predicted when we described the iterative method; in fact, the antisymmetry was the design criterion for the iterative scheme [*Rose*, 2001, 2002]. *Wapenaar et al.* [2012a] show that, for their simple configuration with one dipping layer, convergence is reached after one iteration.
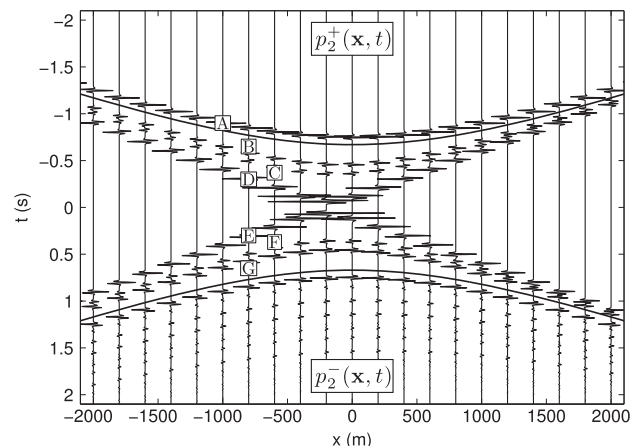

Figure 7. Second iteration of the incident wavefield ($t < 0$) and its reflection response ($t > 0$), both measured at $z = 0$. The labels A–G identify the first seven events in the total field. We show the reflection response only until 2 s.
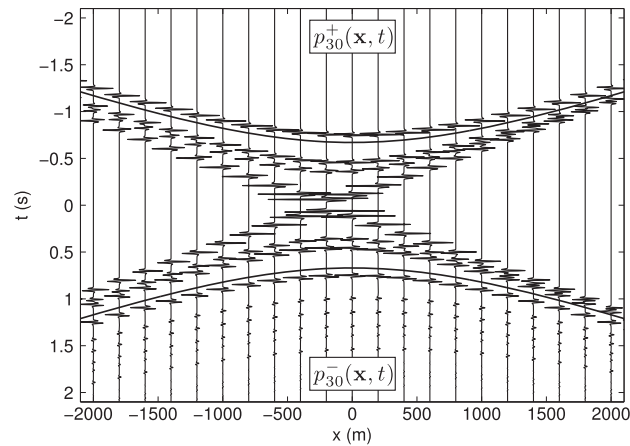
Figure 8. Thirtieth iteration of the incident wavefield ($t < 0$) and its reflection response ($t > 0$), both measured at $z = 0$. Within the solid black lines, the total field is antisymmetric in time and this particular feature was the design criterion for the iterative scheme. The method has converged to the final result.

2.6. Green's Function Retrieval From the Virtual Source

After showing that the method converges to the desired result, we define $p_k(\mathbf{x}, t)$ as the superposition of the kth version of the incident and reflected wavefields: $p_k(\mathbf{x}, t) = p_k^+(\mathbf{x}, t) + p_k^-(\mathbf{x}, t)$. Figures 4, 6, 7, and 8 show $p_k(\mathbf{x}, t)$ at $z = 0$ for $k = 0, 1, 2$, and 30, respectively. For brevity, we define $p(\mathbf{x}, t) = p_{30}(\mathbf{x}, t)$. We remind the reader that, within the solid black lines, the total field at $z = 0$ is antisymmetric in time, and this particular feature was the design criterion for the iterative scheme. Consequently, if we sum the total field and its time-reversed version, i.e., $p(\mathbf{x}, t) + p(\mathbf{x}, -t)$, all events inside the time window cancel each other, as shown in Figure 9. Note that $p(\mathbf{x}, t) + p(\mathbf{x}, -t)$ also obeys the wave equation because we consider a lossless medium. The causal part of this superposition corresponds to $p^-(\mathbf{x}, t) + p^+(\mathbf{x}, -t)$, and the anticausal part is equal to $p^+(\mathbf{x}, t) + p^-(\mathbf{x}, -t)$, as shown in Figure 9 for $t > 0$ and $t < 0$, respectively. From a physical point of view, time reversal changes the propagation direction. Hence, it follows that the causal part propagates upward at $z = 0$ and the anticausal part propagates downward at $z = 0$. According to our theory [*Wapenaar et al.*, 2013], the causal and anticausal parts of Figure 9 are equal to $G(\mathbf{x}, \mathbf{x}_{VS}, t)$ and $G(\mathbf{x}, \mathbf{x}_{VS}, -t)$ for $z = 0$, respectively. This can be understood with the following heuristic derivation. The first event of the causal part of Figure 9 has the same arrival time as the direct arrival of the response to the virtual source at $\mathbf{x}_{VS}$ (Figure 3). If we combine this last observation with the fact that the causal part is upward propagating at $z = 0$ and that the total field obeys the wave equation in the inhomogeneous medium and is symmetric, it can be understood that the total field in Figure 9 is equal to $G(\mathbf{x}, \mathbf{x}_{VS}, t) + G(\mathbf{x}, \mathbf{x}_{VS}, -t)$.

This reasoning does not depend on any particular feature of the configuration used in this analysis, and according to our theory, it indeed holds for more general situations [*Wapenaar et al.*, 2013]. We confirm its
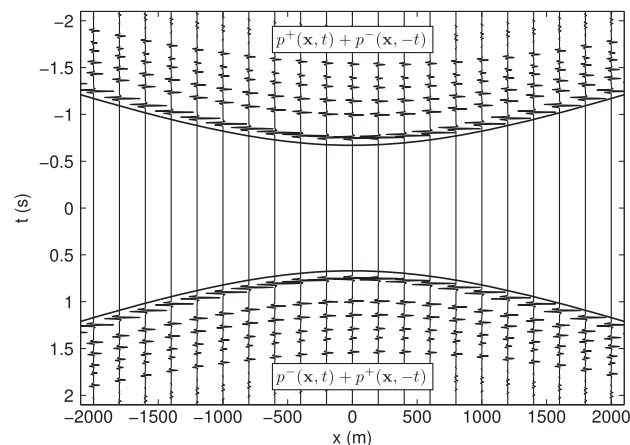

Figure 9. Thirtieth iteration. Superposition of the total field and its time-reversed version after the method has converged.
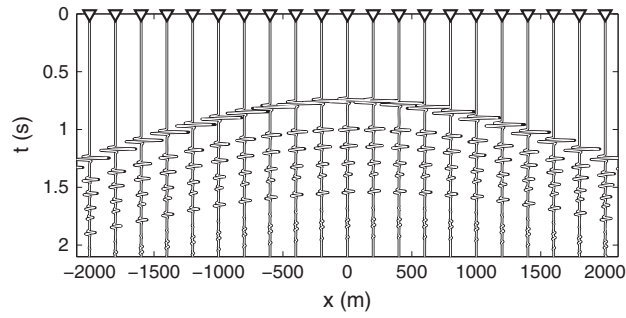
Figure 10. Superposition of the total field originated by a real source located at $\mathbf{x}_{VS}$ (black line) and the wavefield retrieved by the iterative scheme (white line). The two wavefields match perfectly.

validity for the response in Figure 9. Following the steps that led to the field shown in Figure 9, we find for the causal part that

$$
\begin{aligned}
p^-(\mathbf{x}, t) + p^+(\mathbf{x}, -t) = \tau_1^+ \tau_2^+ \tau_1^- \tau_2^- \big\{ & G_0^d(\mathbf{x}, \mathbf{x}_{VS}, t) \\
& + r_3 G_0^d(\mathbf{x}, \mathbf{x}_{VS}^{(4)}, t) - r_1 r_2 G_0^d(\mathbf{x}, \mathbf{x}_{VS}^{(5)}, t) - r_2 r_3 G_0^d(\mathbf{x}, \mathbf{x}_{VS}^{(6)}, t) \\
& - r_1 r_2 r_3 G_0^d(\mathbf{x}, \mathbf{x}_{VS}^{(7)}, t) - r_2 (r_1^2 r_2 - r_3^2) G_0^d(\mathbf{x}, \mathbf{x}_{VS}^{(8)}, t) \dots \big\} * s(t),
\end{aligned}
\tag{11}
$$

with the virtual source position and its mirror images shown in Figure 1. For the configuration of Figure 1, expression (11) is equal to the wavefield $G(\mathbf{x}, \mathbf{x}_{VS}, t) * s(t)$ originated from the virtual source and recorded at the surface. The directly modeled response to the virtual source is shown in Figure 2 and matches the causal part of the field shown in Figure 9. These two wavefields are superposed in Figure 10. This is also illustrated in Figure 11, where we superposed the traces $G(\mathbf{x}_{R0}, \mathbf{x}_{VS}, t) * s(t)$ and $p^-(\mathbf{x}_{R0}, t) + p^+(\mathbf{x}_{R0}, -t)$, where $\mathbf{x}_{R0} = (0, 0)$. For the total wavefield, we obtain

$$
p(\mathbf{x}, t) + p(\mathbf{x}, -t) = G_h(\mathbf{x}, \mathbf{x}_{VS}, t) * s(t),
\tag{12}
$$

where $G_h(\mathbf{x}, \mathbf{x}_{VS}, t) = G(\mathbf{x}, \mathbf{x}_{VS}, t) + G(\mathbf{x}, \mathbf{x}_{VS}, -t)$.

Note that $G(\mathbf{x}, \mathbf{x}_{VS}, -t)$ satisfies the same wave equation as $G(\mathbf{x}, \mathbf{x}_{VS}, t)$, i.e., $LG(\mathbf{x}, \mathbf{x}_{VS}, -t) = -\rho_3 \delta(\mathbf{x} - \mathbf{x}_{VS}) \frac{\partial \delta(-t)}{\partial(-t)} = \rho_3 \delta(\mathbf{x} - \mathbf{x}_{VS}) \frac{\partial \delta(t)}{\partial t}$. Hence, G_h satisfies the homogeneous equation $LG_h = -\rho_3 \delta(\mathbf{x} - \mathbf{x}_{VS}) \frac{\partial \delta(t)}{\partial t} + \rho_3 \delta(\mathbf{x} - \mathbf{x}_{VS}) \frac{\partial \delta(t)}{\partial t} = 0$.

To show the convergence of the proposed method numerically, we compute the energy of $p_k(\mathbf{x}, t) + p_k(\mathbf{x}, -t)$ within the solid black lines as a function of the number of iterations:

$$
\text{Energy}(k) = \sum_t \sum_{\mathbf{x}} w(\mathbf{x}, t) \left[p_k(\mathbf{x}, t) + p_k(\mathbf{x}, -t) \right]^2.
\tag{13}
$$

This quantity is shown in Figure 12, and the energy inside the time window clearly converges to zero, as confirmed by Figure 9. Note that this procedure is expected to converge because in each iteration the reflected energy is smaller than the incident energy. We consider the proposed method as a correction scheme that minimizes the energy within the region where the time window $w(\mathbf{x}, t)$ equals 1. Finally, it
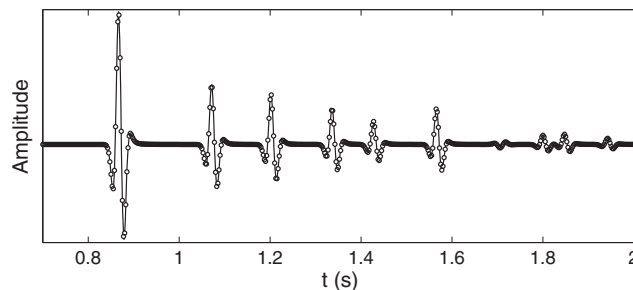

Figure 11. Superposition of $G(\mathbf{x}_{R0}, \mathbf{x}_{VS}, t) * s(t)$ (solid line) and $p^-(\mathbf{x}_{R0}, t) + p^+(\mathbf{x}_{R0}, -t)$ (black circles) for $\mathbf{x}_{R0} = (0, 0)$. The two traces match perfectly.
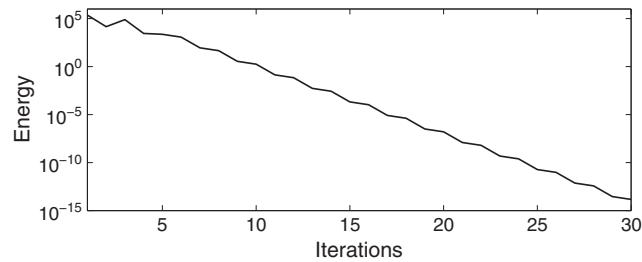
Figure 12. Energy of $p_k(\mathbf{x}, t) + p_k(\mathbf{x}, -t)$ within the region where the time window $w(\mathbf{x}, t)$ equals 1 versus number of iterations k. A logarithmic scale (base 10) is used for the Y axis.

should be noted that we initiated the scheme with $p_0^+(\mathbf{x}, t)$, which, via equations (1), (5), and (6), requires information on the travel time $|\mathbf{x} - \mathbf{x}_{VS}|/c$, as well as on the transmission coefficients of the interfaces and the density of the third layer. When only travel time information is available, the transmission coefficients and mass density in equations (1) and (6) need to be omitted. As a consequence, equation (12) will become

$$p(\mathbf{x}, t) + p(\mathbf{x}, -t) = \frac{\tau_1^+ \tau_2^+}{\rho_3} G_h(\mathbf{x}, \mathbf{x}_{VS}, t) * s(t). \tag{14}$$

This means that the scheme converges to the Green's function, multiplied by a factor $\tau_1^+ \tau_2^+ / \rho_3$, which is of course unknown.

3. Wavefield Decomposition

We first apply a simple source-receiver reciprocity argument, $G(\mathbf{x}_{VS}, \mathbf{x}, t) * s(t) = G(\mathbf{x}, \mathbf{x}_{VS}, t) * s(t)$, and define $G(\mathbf{x}_{VS}, \mathbf{x}, t) * s(t)$ as the wavefield originating from sources at the surface and observed by a virtual receiver located at $\mathbf{x}_{VS}$. Following this reasoning, the wavefield in Figure 2 can be interpreted as the response recorded at the location $\mathbf{x}_{VS}$, indicated by the black dot in Figure 1, due to sources indicated by the white triangles.

To build an image of the reflectors, it is necessary to decompose the total Green's function at the virtual receiver located at $\mathbf{x}_{VS}$ into its downgoing and upgoing components, $G^+(\mathbf{x}_{VS}, \mathbf{x}, t) * s(t)$ and $G^-(\mathbf{x}_{VS}, \mathbf{x}, t) * s(t)$, respectively. These wavefields are illustrated in Figure 13. To perform this decomposition, we consider a

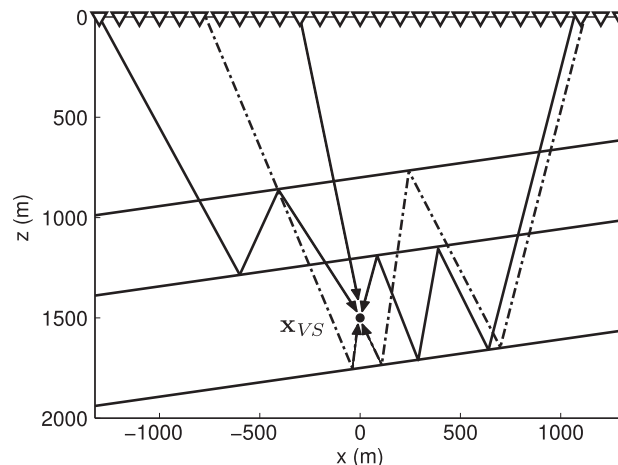**Figure 13.** Total wavefield at the virtual receiver located at $\mathbf{x}_{VS}$. The solid black rays correspond to $G^+(\mathbf{x}_{VS}, \mathbf{x}, t) * s(t)$. The dashed black rays correspond to $G^-(\mathbf{x}_{VS}, \mathbf{x}, t) * s(t)$.
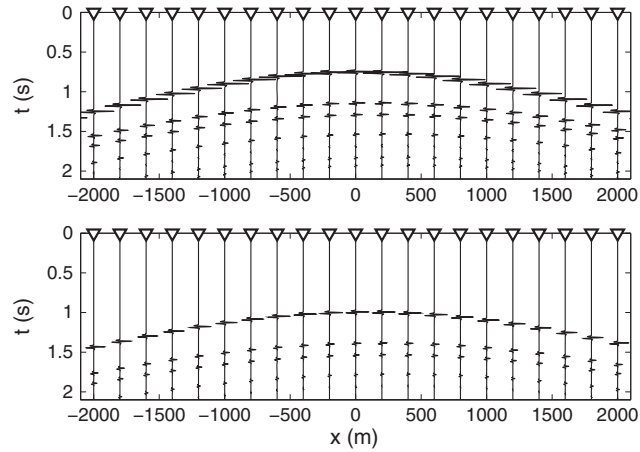
Figure 14. Upgoing and downgoing wavefield decomposition. (top) $G^+(\mathbf{x}_{VS}, \mathbf{x}, t) * s(t)$. (bottom) $G^-(\mathbf{x}_{VS}, \mathbf{x}, t) * s(t)$.

variant of the iterative scheme, in which the subtraction in equation (8) is replaced by an addition [*Wapenaar et al.*, 2011a]:

$$q_k^+(\mathbf{x}, t) = q_0^+(\mathbf{x}, t) + w(\mathbf{x}, t)q_{k-1}^-(\mathbf{x}, -t), \quad \text{for } \mathbf{x} \text{ at } z = 0, \tag{15}$$

where the time window $w(\mathbf{x}, t)$ is defined by equation (2). Note that the 0th iteration of the downgoing field $q_0^+(\mathbf{x}, t)$ is equal to $p_0^+(\mathbf{x}, t)$. As in the previous section, the reflection response is then obtained using equation (9), which we rewrite here as

$$q_k^-(\mathbf{x}_R, t) = \int_{-\infty}^{\infty} \left[R(\mathbf{x}_R, \mathbf{x}, t) * q_k^+(\mathbf{x}, t) \right]_{z=0} d\mathbf{x}, \quad \text{for } z_R = 0. \tag{16}$$

After convergence, we define two additional wavefields: $p_{\text{sym}}(\mathbf{x}, t) = p(\mathbf{x}, t) + p(\mathbf{x}, -t)$ and $p_{\text{asym}}(\mathbf{x}, t) = q(\mathbf{x}, t) - q(\mathbf{x}, -t)$ [*Wapenaar et al.*, 2012b].

Finally, by combining the wavefields $p_{\text{sym}}(\mathbf{x}, t)$ and $p_{\text{asym}}(\mathbf{x}, t)$ in two different ways, the Green's function at $\mathbf{x}_{VS}$ is decomposed into downgoing and upgoing fields, according to

$$G^+(\mathbf{x}_{VS}, \mathbf{x}, t) * s(t) = \frac{1}{2} \left\{ p_{\text{sym}}(\mathbf{x}, t) - p_{\text{asym}}(\mathbf{x}, t) \right\}, \quad \text{for } t \geq 0, \tag{17}$$

and

$$G^-(\mathbf{x}_{VS}, \mathbf{x}, t) * s(t) = \frac{1}{2} \left\{ p_{\text{sym}}(\mathbf{x}, t) + p_{\text{asym}}(\mathbf{x}, t) \right\}, \quad \text{for } t \geq 0. \tag{18}$$

The decomposition of the wavefield observed at the virtual receiver located at $\mathbf{x}_{VS}$ (Figure 10) is shown in Figure 14. Figure 14 (top) corresponds to the downward propagating Green's function $G^+(\mathbf{x}_{VS}, \mathbf{x}, t) * s(t)$, and Figure 14 (bottom) shows the upward propagating Green's function $G^-(\mathbf{x}_{VS}, \mathbf{x}, t) * s(t)$.

4. Imaging
4.1. Standard Prestack Imaging
We start by creating a reference image using a standard imaging technique [*Claerbout*, 1985]. Standard prestack imaging and many other seismic imaging algorithms rely on the single scattering assumption. This implies that the recorded wavefields do not include internal multiples (waves bouncing multiple times between reflectors before reaching the receivers). When multiple reflections are present in the data, the imaging algorithm incorrectly interprets them as ghost reflectors. An initial image, constructed using the conventional approach, is shown in Figure 15a, and the arrows indicate some of the ghost reflectors present in this standard image. Also, note that the amplitudes do not agree with the correct reflection coefficients.
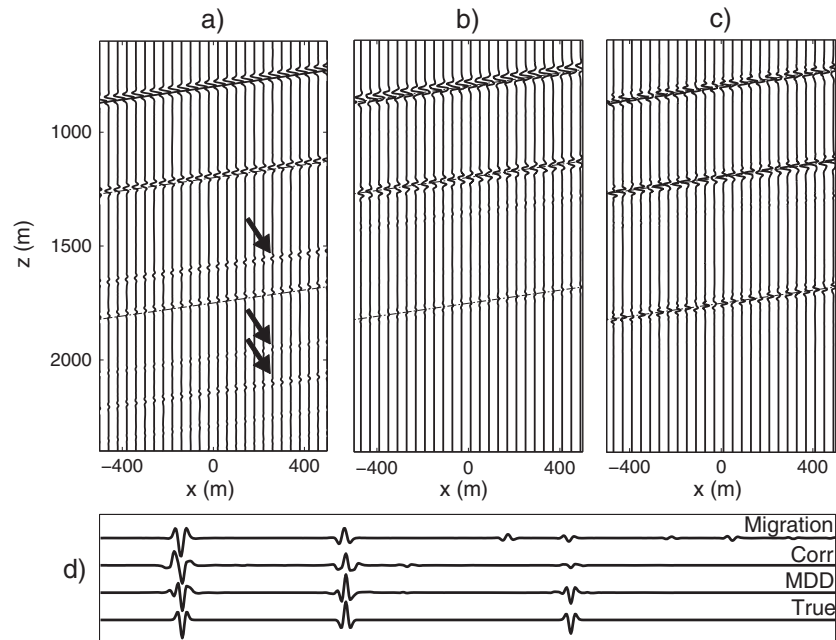
Figure 15. (a) Image of the reflectors obtained with standard prestack migration. The arrows indicate ghost images. (b) Image of the reflectors obtained with the cross-correlation function C. (c) Image of the reflectors obtained with multidimensional deconvolution. (d) Comparison of the reflectivity at $x = 0$ m retrieved by standard prestack migration, cross correlation, and multidimensional deconvolution with the true reflectivity (from top to bottom).

4.2. Imaging With Cross Correlation

If we repeat the decomposition process described in the previous section for virtual receivers $\mathbf{x}_{VS}$ located on many depth levels $z = z_i$ (e.g., the horizontal lines composed of black dots in Figure 16), we are able to create a more accurate image of the medium. To perform this task, we compute the cross-correlation function C

$$C(\mathbf{x}_{VS}, \mathbf{x}_{VS}, t) = \int_{-\infty}^{\infty} \left[G^-(\mathbf{x}_{VS}, \mathbf{x}, t) * G^+(\mathbf{x}_{VS}, \mathbf{x}, -t) \right]_{z=0} dx \tag{19}$$

at every virtual receiver depth and evaluate the result at $t = 0$. This new image is shown in Figure 15b. As in the standard prestack image, the actual reflectors have been reconstructed at the correct spatial location, but now the image is free of internal multiple ghosts. This also holds for more general situations, not only in simple configurations like the one analyzed in this paper (F. Broggini et al., Data-driven wave field focusing and imaging with multidimensional deconvolution: Numerical examples for reflection data with internal multiples, submitted to *Geophysics*, 2014). This is an improvement over the previous image, but the retrieved amplitudes still do not agree with the true reflection coefficients. The amplitude of the first two
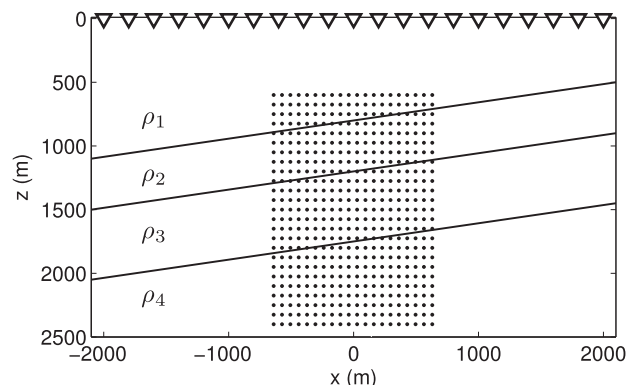

Figure 16. The black dots correspond to various virtual receiver locations $\mathbf{x}_{VS}$. Virtual receivers located on a constant depth level $z = z_i$ are used to resolve $\left[R(\mathbf{x}_r, \mathbf{x}, t) \right]_{z=z_i}$.

reflectors should have the same magnitude and opposite polarity because $r_2 = -r_1$ (in this particular configuration), but the amplitude of the second reflector is smaller than the first one. Furthermore, the amplitude of the third reflector should be 75% of that of the first reflector ($r_3 = 0.75r_1$), but the image shows that the amplitude of the third reflector is considerably smaller than its expected value.

4.3. Imaging With Multidimensional Deconvolution

Now, we show that multidimensional deconvolution allows us to create an image with more accurate amplitudes. As in imaging with cross correlation, we consider a constant depth level $z = z_i$. The Green's functions at this constant depth level are related by

$$G^-(\mathbf{x}_r, \mathbf{x}_s, t) = \int_{-\infty}^{\infty} \left[R(\mathbf{x}_r, \mathbf{x}, t) * G^+(\mathbf{x}, \mathbf{x}_s, t) \right]_{z=z_i} dx, \tag{20}$$

where $R(\mathbf{x}_r, \mathbf{x}, t)$ is the reflection response to downgoing waves at $z = z_i$ of the truncated medium below $z = z_i$, $\mathbf{x}_s$ is at $z = 0$, and $\mathbf{x}_r$ is at $z = z_i$. The truncated medium is equal to the true medium below the depth level $z = z_i$ and is homogeneous above $z = z_i$. Now, the reflectivity $R(\mathbf{x}_r, \mathbf{x}, t)$ can be resolved from equation (20) by multidimensional deconvolution (MDD)[*Wapenaar et al.*,2011b]. To achieve this result, we first correlate both sides of equation (20) with the downgoing Green's function and integrate over source locations over the acquisition surface:

$$C(\mathbf{x}_r, \mathbf{x}', t) = \int_{-\infty}^{\infty} \left[R(\mathbf{x}_r, \mathbf{x}, t) * \Gamma(\mathbf{x}, \mathbf{x}', t) \right]_{z=z_i} dx, \tag{21}$$

for $\mathbf{x}_r$ and $\mathbf{x}'$ at $z = z_i$,

where C is the cross-correlation function (as in the previous section but with noncoinciding coordinates)

$$C(\mathbf{x}_r, \mathbf{x}', t) = \int_{-\infty}^{\infty} \left[G^-(\mathbf{x}_r, \mathbf{x}_s, t) * G^+(\mathbf{x}', \mathbf{x}_s, -t) \right]_{z_s=0} dx_s, \tag{22}$$

and Γ is the point spread function [*van der Neut et al.*, 2011]

$$\Gamma(\mathbf{x}, \mathbf{x}', t) = \int_{-\infty}^{\infty} \left[G^+(\mathbf{x}, \mathbf{x}_s, t) * G^+(\mathbf{x}', \mathbf{x}_s, -t) \right]_{z_s=0} dx_s. \tag{23}$$

We resolve $R(\mathbf{x}_r, \mathbf{x}, t)$ from equation (21) for different depth levels $z = z_i$ and many virtual source locations, as shown by the horizontal lines composed of black dots in Figure 16 and evaluate the result at $t = 0$ and $x_r = x$. Figure 15c shows the final result of the imaging process. As in the previous image, the reflectors have been imaged at the correct spatial locations, but now the retrieved amplitudes agree with the true reflection coefficients. The amplitudes of the first two reflectors have similar magnitude and opposite polarity, and the amplitude of the third reflector is roughly 75% of that of the first reflector. The difference in the amplitudes between the two images is clearly shown in Figure 15d, where we compare the reflectivity as a function of depth at $x = 0$ m, retrieved by standard prestack migration, cross correlation, and multidimensional deconvolution, with the true reflectivity. Multidimensional deconvolution acknowledges the multidimensional nature of the seismic wavefield; hence, the internal multiples contribute to the restoration of the amplitudes of the reflectors. Note that the deconvolution also compensates for unknown factors in the retrieved Green's function, such as in equation (14).

5. Conclusions

We discussed a generalization to two dimensions of the model-independent wavefield retrieval method of *Broggini et al.* [2011, 2012]. Unlike the one-dimensional method, which uses the reflection response only, the proposed multidimensional extension requires, in addition to the reflection response, independent information about the first arrivals. The method can be easily extended to three dimensions.

The proposed data-driven procedure yields the Green's function (including all internal multiples) originating from a virtual source, without needing a receiver at the virtual source location and without needing detailed knowledge of the medium. The method requires (1) an estimate of the direct-arriving wavefront at the surface originated from a virtual source in the subsurface and (2) the reflection impulse responses for all source and receiver positions at the surface. The direct-arriving wavefront can be obtained by modeling in a macro model, from microseismic events [*Artman et al.*, 2010], from borehole check shots, or directly

from the data by, e.g., the common focus point method [*Berkhout*, 1997; *Thorbecke*, 1997; *Haffinger and Verschuur*, 2012] when the virtual source is located at an interface. The required reflection responses are obtained from conventional seismic reflection data after removal of the multiples due to the free surface and after deconvolution for the source wavelet [*Verschuur et al.*, 1992; *Amundsen*, 2001; *Groenestijn and Vershuur*, 2009].

For a simple configuration with planar dipping reflectors, the stationary phase analysis gives a better understanding of the two-dimensional iterative scheme and confirms that the method converges to the virtual-source response. The analysis shows how the multiple-scattering coda of the retrieved wavefield is extracted from the reflection data measured at the surface (which includes all the information about the medium itself).

A variant of the iterative scheme allows the decomposition of the retrieved Green's function into its downgoing and upgoing components. These wavefields are then used to create different images of the medium with cross correlation and multidimensional deconvolution. These two techniques show an improvement over standard imaging and allow us to construct an image that is not affected by ghost images of the reflectors. Additionally, multidimensional deconvolution yields an image whose amplitudes agree with the correct reflection coefficients. This is due to the deconvolution process that correctly handles the internal multiples and retrieves the correct amplitudes of the reflectors. We emphasize that, for the cross correlation and multidimensional deconvolution results, the imaging process does not require any more knowledge of the medium parameters than standard primary imaging schemes (which use a macro model).

The iterative scheme is equivalent to an integral equation. Inserting equation (8) into equation (9) and assuming convergence (setting $p_k^- = p_{k-1}^-$ and then dropping the subscript k) give

$$p^-(\mathbf{x}_R, t) = \int_{-\infty}^{\infty} \left[R(\mathbf{x}_R, \mathbf{x}, t) * p_0^+(\mathbf{x}, t) \right]_{z=0} d\mathbf{x} - \int_{-\infty}^{\infty} \left[R(\mathbf{x}_R, \mathbf{x}, t) * \{ w(\mathbf{x}, t) p^-(\mathbf{x}, -t) \} \right]_{z=0} d\mathbf{x}. \tag{24}$$

This equation is the two-dimensional extension of the Marchenko equation in inverse scattering [*Agranovich and Marchenko*, 1963]. The iterative scheme we propose, thus, implicitly solves the inverse scattering problem. A proof for more general models is given by *Wapenaar et al.* [2013].

Appendix A: Stationary Phase Analysis

We use the method of stationary phase [*Erdélyi*, 1956, *Bleistein and Handelsman*, 1975] to evaluate equation (7), which is repeated here for convenience

$$p_0^-(\mathbf{x}_R, t) = \int_{-\infty}^{\infty} \left[R(\mathbf{x}_R, \mathbf{x}, t) * p_0^+(\mathbf{x}, t) \right]_{z=0} d\mathbf{x}, \tag{A1}$$

with $z_R = 0$. In the frequency domain, this equation reads

$$\hat{p}_0^-(\mathbf{x}_R, \omega) = \int_{-\infty}^{\infty} \left[\hat{R}(\mathbf{x}_R, \mathbf{x}, \omega) \hat{p}_0^+(\mathbf{x}, \omega) \right]_{z=0} d\mathbf{x}, \tag{A2}$$

where the incident downgoing field $\hat{p}_0^+(\mathbf{x}, \omega)$ is defined as $\hat{p}_0^+(\mathbf{x}, \omega) = (\tau_1^+ \tau_1^- \tau_2^+ \tau_2^-)^{-1} \{ \hat{G}^d(\mathbf{x}, \mathbf{x}_{VS}, \omega) \hat{s}(\omega) \}^*$, with the superscript asterisk denoting complex conjugation. Using equation (1) and using the fact that $s(t)$ is symmetric, we have in the high-frequency regime

$$\hat{p}_0^+(\mathbf{x}, \omega) = -j\omega \frac{\rho_3}{\tau_1^+ \tau_2^+} \frac{\exp\{ j(\omega |\mathbf{x} - \mathbf{x}_{VS}|/c + \mu\pi/4) \}}{\sqrt{8\pi |\omega| |\mathbf{x} - \mathbf{x}_{VS}|/c}} \hat{s}(\omega), \tag{A3}$$

with $\mu = \text{sign}(\omega)$. For the reflection impulse response of the medium in Figure 1, we write

$$\hat{R}(\mathbf{x}_R, \mathbf{x}, \omega) = \sum_{n=1}^{\infty} \hat{R}^{(n)}(\mathbf{x}_R, \mathbf{x}, \omega), \tag{A4}$$

where $\hat{R}^{(n)}$ represents the nth event of the reflection response. Using equation (4) we obtain the following high-frequency approximation

$$\hat{R}^{(n)}(\mathbf{x}_R, \mathbf{x}, \omega) = \frac{A^{(n)} z_R^{(n)}}{|\mathbf{x} - \mathbf{x}_R^{(n)}|} \frac{j\omega}{c} \frac{\exp\{ -j(\omega |\mathbf{x} - \mathbf{x}_R^{(n)}|/c + \mu\pi/4) \}}{\sqrt{2\pi |\omega| |\mathbf{x} - \mathbf{x}_R^{(n)}|/c}}. \tag{A5}$$
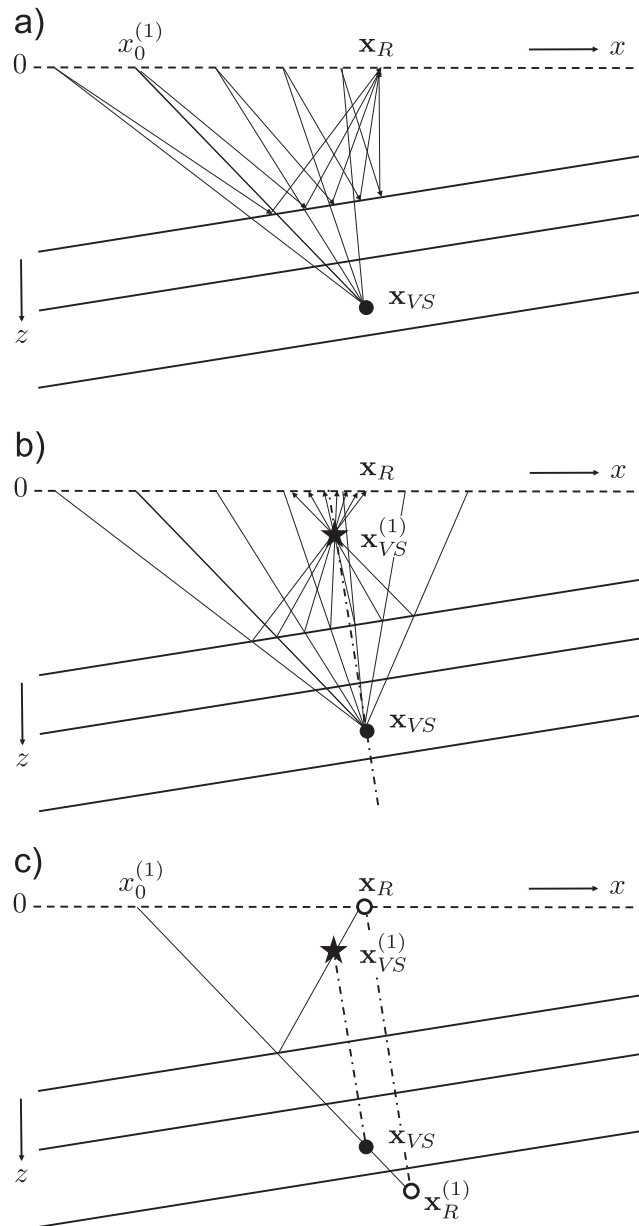
Figure A1. Stationary phase analysis of equation (A1). (a) Analysis of the response of the first reflector for a fixed receiver at $\mathbf{x}_R$. The stationary point is denoted by $x_0^{(1)}$. (b) Stationary rays, like the one in Figure A1a, for different receivers. The response of the first reflector (indicated by the label B in Figure 4) seems to originate from $\mathbf{x}_{VS}^{(1)}$. (c) Geometry underlying equations (A14) and (A18).

For $\hat{R}^{(1)}$, i.e., the primary response of the first reflector, $A^{(1)} = r_1$ and $x_R^{(1)}$ is the mirror image of $\mathbf{x}_R$ with respect to the first reflector. For $\hat{R}^{(2)}$, the primary response of the second reflector, $A^{(2)} = \tau_1^- r_2 \tau_1^+$ and $\mathbf{x}_R^{(2)}$ is the mirror image of $\mathbf{x}_R$ in the second reflector. For $\hat{R}^{(3)}$, the first multiple, $A^{(3)} = -\tau_1^- r_2^2 r_1 \tau_1^+$ and $\mathbf{x}_R^{(3)}$ is the mirror image of $\mathbf{x}_R$ in the mirror image of the first reflector with respect to the second reflector, etc. For $\hat{R}^{(4)}$, the primary response of the third reflector, $A^{(4)} = \tau_1^- \tau_2^- r_3 \tau_2^+ \tau_1^+$ and $\mathbf{x}_R^{(4)}$ is the mirror image of $\mathbf{x}_R$ in the third reflector.

First, we consider the response of the first reflector. Figure A1a shows a number of rays of $R^{(1)}(\mathbf{x}_R, \mathbf{x}, t)$, leaving different sources at the surface, reflecting at the first reflector, and arriving at one and the same receiver at $\mathbf{x}_R$. According to equation (A1), these reflection impulse responses are convolved with the initial incident field, of which the rays are also shown in Figure A1a (these are the rays that converge at $\mathbf{x}_{VS}$). This convolution product is stationary for the source at $x_0^{(1)}$, where the rays of the incident field and of the reflection impulse response have the same direction. Figure A1b shows a number of such stationary rays for different

receiver positions. With simple geometrical arguments, it follows that these rays cross each other at the mirror image of the virtual source with respect to the first reflector, i.e., at $x_{VS}^{(1)} = (-196, 128)$. The travel times of the convolution product are given by the lengths of the rays from $x_{VS}^{(1)}$ to the surface, divided by the velocity. Hence, it is as if the response of the first reflector to the initial incident field originates from a source at $x_{VS}^{(1)}$ (this is confirmed below). Similarly, the response of the second reflector to the initial incident field apparently originates from a mirror image of the virtual source in the second reflector, i.e., at $x_{VS}^{(2)} = (-84, 912)$. The multiple-reflected responses to the initial incident field also apparently originate from mirror images of the virtual source, all located along the line $z = z_{VS} + x/a$, see Figure 1. For example, the first multiple apparently originates from $x_{VS}^{(3)} = (28, 1696)$ (being the mirror image of x_{VS} in the mirror image of the first reflector with respect to the second reflector).

Equation (A2), with $\hat{p}_0^+(x, \omega)$ and $\hat{R}(x_R, x, \omega)$ defined in equations (A3)–(A5), can be written as

$$\hat{p}_0^-(x_R, \omega) = \sum_{n=1}^{\infty} \mathcal{I}^{(n)}, \tag{A6}$$

with

$$\mathcal{I}^{(n)} = \int_{-\infty}^{\infty} f(x) \exp\{jk\phi(x)\} dx, \tag{A7}$$

where $k = \omega/c$,

$$f(x) = \frac{\rho_3}{\tau_1^+ \tau_2^+} \frac{|\omega| A^{(n)} z_R^{(n)} \hat{s}(\omega)}{4\pi l_{VS}^{1/2} \{l_R^{(n)}\}^{3/2}}, \quad \phi(x) = l_{VS} - l_R^{(n)}, \tag{A8}$$

with

$$l_{VS}(x) = |x - x_{VS}| = \sqrt{(x - x_{VS})^2 + z_{VS}^2}, \tag{A9}$$

$$l_R^{(n)}(x) = |x - x_R^{(n)}| = \sqrt{(x - x_R^{(n)})^2 + (z_R^{(n)})^2}. \tag{A10}$$

According to the method of stationary phase [*Erdélyi*, 1956, *Bleistein and Handelsman*, 1975], we may approximate $\mathcal{I}^{(n)}$ for large $|k|$ by

$$\mathcal{I}^{(n)} \approx \sqrt{\frac{2\pi}{|k\phi''(x_0^{(n)})|}} f(x_0^{(n)}) \exp\{j(k\phi(x_0^{(n)}) + \mu\pi/4)\}, \tag{A11}$$

where $x_0^{(n)}$ is the stationary point, i.e, $\phi'(x_0^{(n)}) = 0$. The derivatives of the phase are

$$\phi'(x) = \frac{x - x_{VS}}{l_{VS}} - \frac{x - x_R^{(n)}}{l_R^{(n)}}, \tag{A12}$$

$$\phi''(x) = \frac{z_{VS}^2}{l_{VS}^3} - \frac{(z_R^{(n)})^2}{\{l_R^{(n)}\}^3}. \tag{A13}$$

The point $x_0^{(1)}$ depicted in Figure A1c obeys

$$\frac{x_0^{(1)} - x_{VS}}{z_{VS}} = \frac{x_0^{(1)} - x_R^{(1)}}{z_R^{(1)}}. \tag{A14}$$

Generalized for $x_0^{(n)}$, this gives

$$x_0^{(n)} = \frac{x_{VS} z_R^{(n)} - x_R^{(n)} z_{VS}}{z_R^{(n)} - z_{VS}}. \tag{A15}$$

Substituting this for x into equation (A12) gives $\phi'(x_0^{(n)}) = 0$; hence, $x_0^{(n)}$ is indeed the stationary point of $\phi(x)$. According to equations (A9) and (A10), we have

$$l_{VS}(x_0^{(n)}) = \frac{z_{VS}}{z_R^{(n)} - z_{VS}} |\mathbf{x}_R^{(n)} - \mathbf{x}_{VS}|, \tag{A16}$$

$$l_R^{(n)}(x_0^{(n)}) = \frac{z_R^{(n)}}{z_R^{(n)} - z_{VS}} |\mathbf{x}_R^{(n)} - \mathbf{x}_{VS}|. \tag{A17}$$

Above, we defined $\mathbf{x}_{VS}^{(n)}$ as a mirror image of $\mathbf{x}_{VS}$, obtained in the same way as $\mathbf{x}_R^{(n)}$ is obtained by mirroring $\mathbf{x}_R$. This implies that

$$|\mathbf{x}_R^{(n)} - \mathbf{x}_{VS}| = |\mathbf{x}_R - \mathbf{x}_{VS}^{(n)}|. \tag{A18}$$

This is illustrated for $n = 1$ in Figure A1c. Hence, equation (A11) gives (for large $|k|$)

$$\mathcal{I}^{(n)} \approx j\omega A^{(n)} \frac{\rho_3}{\tau_1^+ \tau_2^+} \frac{\exp\{-j(\omega|\mathbf{x}_R - \mathbf{x}_{VS}^{(n)}|/c + \mu\pi/4)\}}{\sqrt{8\pi|\omega||\mathbf{x}_R - \mathbf{x}_{VS}^{(n)}|/c}} \hat{s}(\omega). \tag{A19}$$

Hence,

$$\hat{p}_0^-(\mathbf{x}_R, \omega) = \sum_{n=1}^{\infty} \mathcal{I}^{(n)} = \sum_{n=1}^{\infty} A^{(n)} \hat{G}_0^d(\mathbf{x}_R, \mathbf{x}_{VS}^{(n)}, \omega)\hat{s}(\omega), \tag{A20}$$

with $\hat{G}_0^d(\mathbf{x}_R, \mathbf{x}_{VS}^{(n)}, \omega)$ as defined in equation (6) but with the source at $\mathbf{x}_{VS}^{(n)}$. In the time domain, this becomes

$$p_0^-(\mathbf{x}_R, t) = \sum_{n=1}^{\infty} A^{(n)} G_0^d(\mathbf{x}_R, \mathbf{x}_{VS}^{(n)}, t) * s(t); \tag{A21}$$

see Figure 4 for $t > 0$.

References

Agranovich, Z. S., and V. A. Marchenko (1963), *The Inverse Problem of Scattering Theory*, Gordon and Breach, New York.

Amundsen, L. (2001), Elimination of free-surface related multiples without need of the source wavelet, *Geophysics*, *66*(1), 327–341.

Artman, B., I. Podladtchikov, and B. Witten (2010), Source location using time-reverse imaging, *Geophys. Prospect.*, *58*(5), 861–873.

Bakulin, A., and R. Calvert (2006), The virtual source method: Theory and case study, *Geophysics*, *71*(4), SI139–SI150.

Berkhout, A. J. (1987), *Applied Seismic Wave Theory*, Elsevier, Amsterdam, Netherlands.

Berkhout, A. J. (1997), Pushing the limits of seismic imaging, Part I: Prestack migration in terms of double dynamic focusing, *Geophysics*, *62*(3), 937–954.

Bleistein, N., and R. A. Handelsman (1975), *Asymptotic Expansions of Integrals*, Dover Publications, Mineola, New York.

Broggini, F., and R. Snieder (2012), Connection of scattering principles: A visual and mathematical tour, *Eur. J. Phys.*, *33*, 593–613.

Broggini, F., R. Snieder, and K. Wapenaar (2011), Connection of scattering principles: Focusing the wavefield without source or receiver, *SEG Tech. Program Expanded Abstr.*, *757*, 3845–3850, doi:10.1190/1.3628008..

Broggini, F., R. Snieder, and K. Wapenaar (2012), Focusing the wavefield inside an unknown 1D medium: Beyond seismic interferometry, *Geophysics*, *77*(5), A25–A28.

Claerbout, J. F. (1985), *Imaging the Earth's Interior*, Blackwell Scientific Publications, Oxford, U.K.

Curtis, A., P. Gerstoft, H. Sato, R. Snieder, and K. Wapenaar (2006), Seismic interferometry—Turning noise into signal, *Leading Edge*, *25*(9), 1082–1092.

de Hoop, A. T. (1995), *Handbook of Radiation and Scattering of Waves*, Academic Press, London, U.K.

Erdélyi, A. (1956), *Asymptotic Expansions*, Dover Publications, Mineola, New York.

Groenestijn, G. J. A. v., and D. J. Verschuur (2009), Estimation of primaries and near-offset reconstruction by sparse inversion: Marine data applications, *Geophysics*, *74*(6), R119–R128.

Haffinger, P., and D. J. Verschuur (2012), Estimation and application of near-surface full waveform redatuming operators, *Geophys. Prospect.*, *60*(2), 270–280.

Keho, T. H., and P. G. Kelamis (2012), Focus on land seismic technology: The near-surface challenge, *Leading Edge*, *32*, 62–28.

Rose, J. H. (2001), "Single-sided" focusing of the time-dependent Schrödinger equation, *Phys. Rev. A*, *65*(1), 012707.

Rose, J. H. (2002), Single-sided autofocusing of sound in layered materials, *Inverse Prob.*, *18*, 1923–1934.

Sava, P., and B. Biondi (2004), Wave-equation migration velocity analysis. II: Subsalt imaging example, *Geophys. Prospect.*, *52*, 607–623.

Schuster, G. T. (2009), *Seismic Interferometry*, Cambridge Univ. Press, Cambridge, U.K.

Snieder, R. (2004), *A Guided Tour of Mathematical Methods for the Physical Sciences*, 2nd edn, Cambridge Univ. Press, Cambridge, U.K.

Thorbecke, J. (1997), Common focus point technology, PhD thesis, Delft Univ. Technology, Delft, Netherlands.

van der Neut, J., J. Thorbecke, K. Mehta, E. Slob, and K. Wapenaar (2011), Controlled-source interferometric redatuming by crosscorrelation and multidimensional deconvolution in elastic media, *Geophysics*, *76*(4), SA63–SA76.

Verschuur, D. J., A. J. Berkhout, and C. P. A. Wapenaar (1992), Adaptive surface-related multiple elimination, *Geophysics*, *57*(9), 1166–1177.

Wapenaar, K., and A. J. Berkhout (1993), Representations of seismic reflection data. Part I: State of affairs, *J. Seism. Explor.*, *2*, 123–131.

Wapenaar, K., D. Draganov, R. Snieder, X. Campman, and A. Verdel (2010), Tutorial on seismic interferometry. Part 1: Basic principles and applications, *Geophysics*, *75*(5), 75A195–75A209.

Wapenaar, K., F. Broggini, and R. Snieder (2011a), A proposal for model-independent 3D wave field reconstruction from reflection data, *SEG Tech. Program Expanded Abstr.*, *746*, 3788–3792, doi:10.1190/1.3627995..

Wapenaar, K., J. van der Neut, E. Ruigrok, D. Draganov, J. Hunziker, E. Slob, J. Thorbecke, and R. Snieder (2011b), Seismic interferometry by crosscorrelation and by multi-dimensional deconvolution: A systematic comparison, *Geophys. J. Int.*, *185*, 1335–1364.

Wapenaar, K., F. Broggini, and R. Snieder (2012a), Creating a virtual source inside a medium from reflection data: Heuristic derivation and stationary-phase analysis, *Geophys. J. Int.*, *190*(2), 1020–1024.

Wapenaar, K., J. Thorbecke, J. van der Neut, E. Slob, F. Broggini, J. Behura, and R. Snieder (2012b), Integrated migration and internal multiple elimination, *SEG Tech. Program Expanded Abstr.*, *707*, 1–5, doi:10.1190/segam2012-1298.1.

Wapenaar, K., F. Broggini, E. Slob, and R. Snieder (2013), Three-dimensional single-sided Marchenko inverse scattering, data-driven focusing, green's function retrieval, and their mutual relations, *Phys. Rev. Lett.*, *110*(8), 084301.